COBEM 2023 27TH INTERNATIONAL CONGRESS OF MECHANICAL ENGENEERING

ABCM Brazilian Society of Mechanical Sciences and Engineering
27th ABCM International Congress of Mechanical Engineering
December 04-08, 2023, Florianópolis-SC, Brazil

# COB-2023-1723
# A COMPARATIVE ANALYSIS OF AUTOMATED CONTACT ANGLE MEASUREMENT METHODS FOR X-RAY MICROTOMOGRAHPIC IMAGES OF TWO-PHASE FLOW IN POROUS MEDIA

**Christoph Indiana Zevenbergen**
**Ricardo Leite Martins Bazarin**
**Diogo Nardelli Siebert**
**Luis Orlando Emerich Santos**
Joinville Technological Center, University of Santa Catarina, R. Dona Francisca 8300 - Bloco U, 89219-600, Joinville, Brazil
christoph.iz@grad.ufsc.br, ricardo.bazarin@posgrad.ufsc.br, diogo.siebert@ufsc.br, emerich@lmpt.ufsc.br

***Abstract.*** *Although an essential parameter for understanding the multicomponent immiscible fluid flow in oil recovery processes, realistic measurements of the wettability in reservoir rock samples is a difficult challenge due to the complexity and heterogeneity of these porous media. With advances in X-ray microtomography, the interactions of wetting and no-wetting fluids with the solid matrix of porous samples can now be observed on the pore scale, enabling in situ measurement of the contact angle even in reservoir conditions. In recent years, the measurement of contact angles through three-dimensional microtomographic images has advanced from manual measurement methods to automated methods that incorporate interface tracking and image data processing. Moreover, accurately estimating contact angles at low-resolution points remains a challenge even for the most advanced techniques. In this context, the present work compares different automated angles methods available in the literature. All the methods examined in this study are employed by codes provided on the GitHub researcher's pages or through our own code implementations, also available on GitHub. We employed a static spherical oil droplet over an inclined plane solid surface as a benchmark problem. For each model, different droplet resolutions, radii, and inclination angles. Finally, the interface tracking techniques are compared and classified regarding their implementation characteristics, computational costs, and accuracy.*

***Keywords:*** *Wettability, Contact angle, Automated measurement, Microtomography*

## 1. INTRODUCTION

Wettability is a crucial parameter on the multiphase flow behavior through porous media. Its influence extends across a wide range of fields, such as enhanced oil recovery (Andrew *et al.*, 2014), remediation of groundwater contamination (Francisca and Montoro, 2015), and geological carbon dioxide capture and storage(Chalbaud *et al.*, 2009). A key aspect of multiphase behavior lies in measuring the contact angle, which characterizes the wetting behavior and fluid distribution at fluid-solid interfaces within porous media.

Until recent years, contact angle measurements were limited to the use of goniometers and other experimental techniques. But through advances in X-ray microtomography in a pioneering study, Andrew *et al.* (2014) demonstrated the feasibility of using microtomography images to manually measure the contact angle within porous media. In the case of porous samples obtained from the reservoir, this approach facilitates the replication of in situ contact angle measurements while considering the intricate irregularities and chemical variations present on the porous surface.

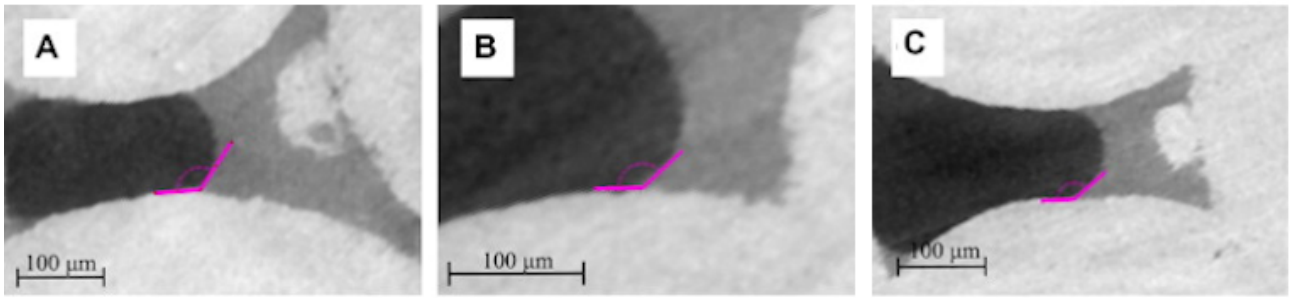


Figure 1. Manual measurement of contact angle. Adapted from Andrew *et al.* (2014).

Since then, some numerical methods have been developed to automate the contact angle measurement in porous media through X-ray microtomography images. Methods developed in recent years have been a useful tool in various

investigations to better understand the distribution of fluids in situ for different values of temperature, pressure, salinity, etc. (Klise *et al.*, 2016).

A variety of automated methods have been proposed to calculate contact angles distribution through the porous media, each offering unique approaches and advancements in the field. The first to propose an automated method was Klise *et al.* (2016) in which he developed a tracking system for the interfaces and calculated the contact angle by fitting planes to the voxelized interfaces. At the same time, McClure *et al.* (2016) proposed a method using second-order finite difference in a distance-signed function to calculate the normal vectors of the surface and the contact angle. Not long after, Scanziani *et al.* (2017) built his method upon the manual approach initially formulated by Andrew *et al.* (2014), where the contact angle was measured by fitting lines and circles in the interfaces on a bi-dimensional image in the plane perpendicular to the contact line. AlRatrout *et al.* (2017) tackled the challenges of image discretization using an iterative smoothing process by interpolating the fluid/fluid and solid/fluid interfaces to better measure the angle using the normal vectors of the interfaces. By tracking the fluid-fluid and fluid-solid interfaces with the level set method, Yang and Zhou (2020) utilized the third-order weighted essentially non-oscillatory (WENO) scheme and Godunov's method for up-winding. Both methods were used to compute the normal vector and determine the contact angle. In further research Ibekwe *et al.* (2020) added new ideas of the contact angle measurement following a method similar to the one developed by Klise *et al.* (2016). Another approach to the problem was adopted by Rabbani *et al.* (2023) who utilized deep learning techniques to measure the contact angle and promised a significant reduction in computational costs. Finally, Zang *et al.* (2023) studied contact angle estimation in bi-dimensional images, by fitting lines and circles to the interfaces. These diverse approaches contribute to the advancement and understanding of contact angle calculation, addressing various challenges, and offering novel insights into contact angle estimation methodologies. However, none of these works provides quantitative and qualitative comparisons between the previously developed models.

Based on the diversity of the models available in the literature, the present work has the objective of analyzing these methods for in situ contact angle measurement, comparing their efficiency and precision. While we were able to obtain the code for the method proposed by McClure *et al.* (2016) (LBPM routine: lbpm_TwoPhase_analysis, `https://github.com/opm/lbpm`), AlRatrout *et al.* (2017) (`https://github.com/AhmedAlratrout/ContactAngle-Curvature-Roughness`) and Rabbani *et al.* (2023) (`https://github.com/ArashRabbani/DeepAngle`), allowing us to directly utilize their approach in our analysis. Other methods, such as those developed by Klise *et al.* (2016) and Scanziani *et al.* (2017), did not have their code readily accessible. Consequently, we developed our own custom code by carefully studying the methodologies outlined in these articles, ensuring that we maintained consistency with the original approaches.

## 2. METHODOLOGY

To compare the methods, a benchmark test was conducted to analyze the errors involved in each approach. By evaluating and contrasting these methodologies, we aim to gain insight into their strengths, limitations, and overall performance in estimating contact angles in porous media. One of the most important characteristics of the method is being able to accurately measure the contact angle in low-resolution images. This becomes especially significant because of the challenge of microtomography images that capture small scales and exceptionally small pore sizes.

### 2.1 Benchmark test

The benchmark test consists of creating synthetic images with pre-defined resolutions and contact angles. In this way, it is possible to compare the true value of contact angle with the contact angle measured, allowing to precisely identify the magnitude of the error involved in each resolution. It is important to note that this approach to quantifying the errors of each method may be biased and does not represent the contact angle error observed in real porous media measurement.

There are many ways to create a synthetic image with contact angles, the most utilized is a perfect droplet sphere in contact with a flat surface, which may be inclined or horizontal. In this work, three benchmark types of images have been used: the horizontal surface P-Z case, given by $z = cte$; and two inclined surfaces P-ZX and P-ZXY cases, given by $z = -x + cte$ and $z = -x - y + cte$, respectively. Figure 2 illustrates the benchmark cases. It is important to note that the constant in the plane equation must be so that the plane fits in between the voxels in such a way that it obeys the given relation: $cte = n + 0.5$ where $n$ is an integer.

The images were created defining the desired contact angle, the image size, and the radius of the sphere, which are both proportional to the image resolution. The resolution is defined by the dimensionless voxel size, which is obtained by dividing the dimensionless droplet diameter by the number of voxels in diameter, as depicted in Figure 2 for the case of 1/28$^{\text{th}}$. To generate the sphere, a reference point on the surface of the plane is needed, and the center of the sphere can be calculated as given:

$$\vec{C} = \vec{P} + \vec{n_p} \cdot R \cdot \cos\theta \tag{1}$$

where $\vec{C}$ is the position of the center of the sphere, $\vec{P}$ a reference point on the surface of the plane, $\vec{n_p}$ is the unit normal vector of the plane, $R$ the radius of the sphere and $\theta$ the contact angle desired. Once the center of the sphere is defined,

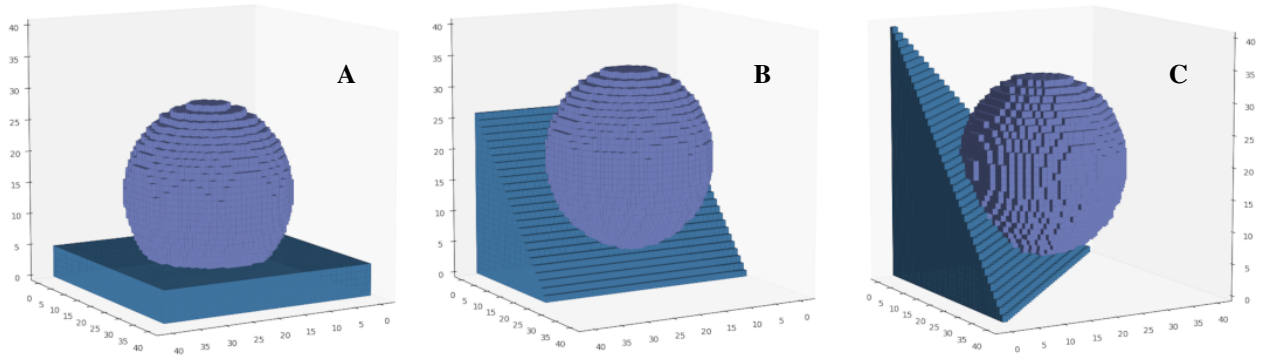


Figure 2. Droplet images with resolution of 1/28th and contact angle of 45°for the cases: P-Z (A) horizontal surface $z = 4.5$ ; P-ZX (B) surface defined by $z = -x + 25.5$; and P-ZXY (C) surface defined by $z = -x - y + 39.5$.

the voxels of the image inside the sphere and outside the solid volume are defined as fluid 1, and the remaining volumes are defined as fluid 2.

### 2.2 Automated contact angle methods

Regardless of the specific approach employed by each methodology, all techniques follow a common structure comprising four general steps:

1. Tracking the rock-fluid and fluid-fluid interfaces, as well as the three-phase contact lines and points. Taking into account the connectivity process applied to the segmented image, it is possible to use 6, 18, and 26 voxels connectivity for 3D images.

2. Image processing around the contact line and interfaces. As example, points interpolation and smoothing process of planes.

3. Utilizing the processed information to calculate parameters, such as surface normal vectors and interface plane equations.

4. Calculating the contact angle, most commonly by taking the scalar product of the normal vectors of the fluid-fluid interface and the rock-fluid interface, as given by

$$\theta = \pi - \arccos\left(\vec{n_1} \cdot \vec{n_2}\right). \tag{2}$$

However, the distinct approaches used in the described steps by each method result in varying precision for determining the values of contact angle. Consequently, each method compared in this study is analyzed concerning its measurement aspects and implementation.

#### 2.2.1 2D fitted lines methodology

Scanziani *et al.* (2017) automated the manual process first developed by Andrew *et al.* (2014) to calculate the in situ contact angle of porous media. In this method, the angle is measured by fitting lines to the interface in a bi-dimensional image. The first step of this method is to track the contact line (Fig. 3 **A**) and then smooth it using a moving average procedure considering a cubic sub-volume region with size of $a$ and a number of points used equal to $N$. This is necessary to better approximate the perpendicular plane to the contact curve where the contact angle is going to be measured (Fig. 3 **B**). From the perpendicular plane, a two-dimensional image is captured and lines are fitted to the rock-fluid and fluid-fluid interfaces using a linear regression method (Fig. 3 **C**). The rock-fluid interface is defined by the rock pixels connected to other phases, with $\ell$ representing the pixel length of the interface, and the fluid-fluid interface is defined by the fluid 1 pixels connected to fluid 2, with $b$ denoting the length of the cubic sub-volume considered for the fluid-fluid interface. Both $\ell$ and $b$ are required as input parameters. In the fluid-fluid interface, a circle is fitted to conform to the constant curvature defined by the Young-Laplace equation for fluid interfaces under equilibrium conditions. The values of the circle's center and its curvature are obtained using the least squares method. Once the circle and line functions are determined for the interfaces, the contact angle is calculated as the angle between the rock-fluid interface and the tangent line of the fluid-fluid interface at the contact point.

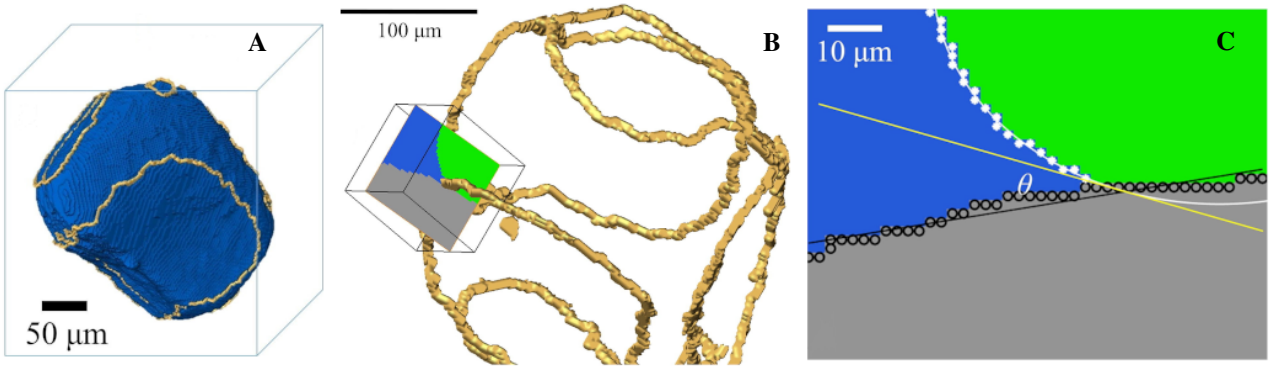


Figure 3. Steps of the automated contact angle measurement: **A** track the three-phase contact points; **B** Setting the normal plane; **C** Adjusting the lines that better fit the interface points. Adapted from Scanziani *et al.* (2017).

For the application of Scanziani *et al.* (2017) methodology, was employed the Python code available on the GitHub page (`https://github.com/alessioscanziani/contact-angle-python`). The author's proposed numerical measurement is aided by the commercial software `Thermofisher Avizo 9.5` in two steps: tracking the rock-fluid and fluid-fluid interfaces, as well as the contact line; and extracting the two-dimensional images perpendicular to the contact curve. In this work, we replaced the processes typically carried out with `Thermofisher Avizo 9.5` with Python code routines. The tracking of the rock-fluid, fluid-fluid, and contact line regions is performed in a consistent manner, employing a connectivity process of 6 voxels as recommended by the author. Additionally, the extraction of two-dimensional images perpendicular to the contact curve is achieved using an algebraic plane approximation, which relies on the normal vector determined by the author's code. The complete Python code for the automated contact angle measurement method is available on the GitHub page (`https://github.com/poro-labcc/Contact_Angle_Measurement-Scanziani Version-PythonCode-COBEM`)). The input parameters $a$, $N$, $\ell$ and $b$ were set in 15, 5, 200 and to the length of the benchmark image, respectively.

### 2.2.2 Level set method

Building upon the Level Set interface tracking method, McClure *et al.* (2016) developed an automated tool for measuring contact angles by computing gradients at the interfaces. Equation (3) describes the level set function:

$$\frac{\partial \phi}{\partial t} + \zeta \cdot |\nabla \phi| = 0 \quad \rightarrow \quad \phi = \frac{\rho_n - \rho_w}{\rho_n + \rho_w} \tag{3}$$

where $\zeta$ is the normal vector of the velocity, $\phi$ is the level set function, $\rho$ the density, and $n$ and $w$ the subscripts for non-wetting and $w$ wetting fluid, respectively. For the measurement of the contact angle, the stationary regime is considered, i.e., $|\nabla \phi| = 0$. To compute the derivative terms is employed a second order finite-difference method. Through the normal vector at the $s - w$ ($\vec{n}_s$) and $w - n$ ($\vec{n}_w$) interfaces, i.e., taking the wetting fluid as a reference, the contact angle is calculated by $\theta = \pi - \arccos(\vec{n_w} \cdot \vec{n_s})$. It is important to clarify that no input parameters are required for the measurement methodology. The contact angle measurement is performed using the lbpm_TwoPhase_analysis routine available in the LBPM software (accessible at `https://github.com/opm/lbpm`), following the instructions provided in the user guide (`https://lbpm-sim.org/examples/analysis/TwoPhase.html`).

### 2.2.3 Fitted planes methodology

By measuring the angle between the fitted planes, Klise *et al.* (2016) proposed using a linear plane approximation to locally determine contact angles in segmented data. Initially, an image tracking process identifies the interfaces and contact points through point-to-point connectivity. An interface is defined where two voxels of different types are connected, while a contact point is defined where all types of voxels (fluid1, fluid2, and rock) are connected. All interfaces and contact points are determined using only one fluid phase as a reference, as illustrated in Figure 4 (A). At the contact point, a set of points for each interface (fluid-fluid and fluid-rock) is collected within a specified search radius. The planes are fitted to the collected set of points (Figure 4 B), and the contact angle is calculated using the dot product of the normal vectors of the planes (Eq. 2).

Klise *et al.* (2016) conducted a sensitivity analysis on the parameters of connectivity, search radius for the collected points around the contact point, and the minimum number of points around the contact point necessary for a optimized plane fit. The droplet case is used on the double inclined surface (Figure 2 C) for analysis. Based on those results, we opted to use a connectivity of 6 and a search radius of 4 for the resolutions of 1/14$^{\text{th}}$, 1/28$^{\text{th}}$ and 1/56$^{\text{th}}$, and a search radius of 5 for resolution of 1 /112$^{\text{th}}$.

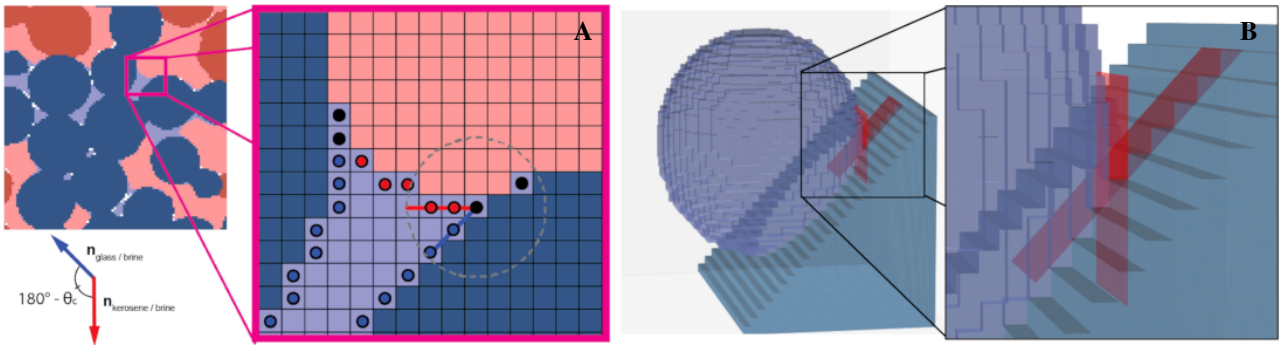


Figure 4. Segmented data interpretation: (**A**) bi-dimensional visualisation of interfaces and contact points; (**B**) plane fitting in set of points. Adapted from Klise *et al.* (2016).

In this work, the methodology proposed by Klise *et al.* (2016) has been implemented in a Python code, following the steps described above. Since the article lacks specific information on the process used to fit the planes, we utilized a least-squares solution to linear matrix equations. The code does not require input measurement parameters and is available on page (`https://github.com/poro-labcc/Contact_Angle_Measurement-KliseVersion-PythonCode-COBEM`).

### 2.2.4 Volume-preserving smoothing

AlRatrout *et al.* (2017) proposed a new approach to treat and measure contact angles in segmented data from porous media. By using Gaussian smoothing on the interfaces, it aims to eliminate limitations related to image resolution while preserving the volume of each phase. The first step involves identifying the fluid-fluid and fluid-rock interfaces based on the faces of the voxels and locating the contact points using the edge lines and vertices that connect three different phase voxels (Fig. 5 A). Subsequently, a volume-preserving Gaussian smoothing process is applied iteratively to smooth the interface, preventing the mesh volume from shrinking (Fig. 5 B). The input parameters for the Gaussian smoothing step include the Gaussian relaxation factor ($\beta$), Gaussian relaxation factor ($R_{Gauss}$), and Gaussian iterations necessary to converge the process. The final step is the iterative smoothing of the interface curvature, where the fluid-fluid interfaces are adjusted to reduce curvature variations while preserving the volume of the fluids (Fig. 5 C). The input parameters for the volume-preserving curvature smoothing step include the curvature relaxation factor ($\gamma$), the curvature relaxation factor ($R_\kappa$), and the curvature iterations necessary to converge the process. After all the steps, the contact angles are calculated at the vertices of the contact lines by taking the dot product of the normal vectors of the edges (Fig. 5 D).

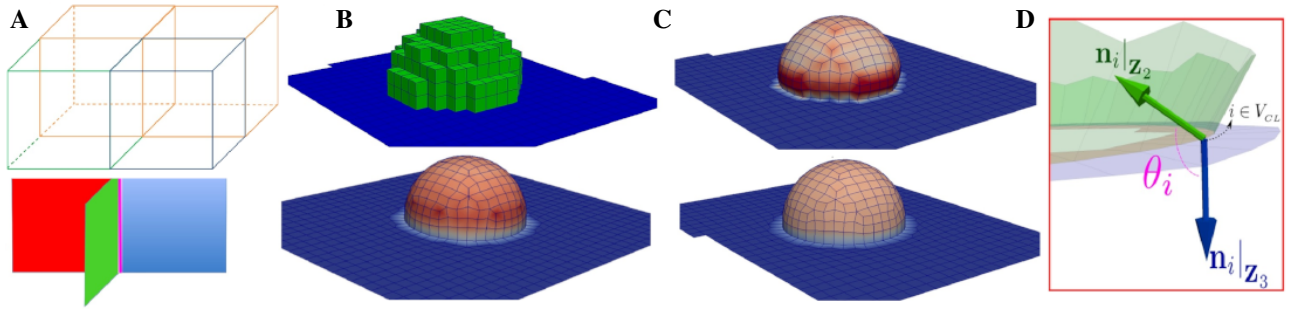


Figure 5. Process of AlRatrout *et al.* (2017) methodology: (**A**) Quadrilateral simplicial complex domain for tracking interfaces, edges, and vertices; (**B**) volume-preserving Gaussian smoothing step; (**C**) volume-preserving curvature smoothing step; (**D**) normal vectors to edges at the contact line vertex. Adapted from AlRatrout *et al.* (2017).

The present work follows the implementation of software available on the page (`https://github.com/AhmedAlratrout/ContactAngle-Curvature-Roughness`). The input parameters for the performed cases are set following the optimal values suggested by the author: $\beta = 0.1$, $R_{Gauss} = 3$, 40 Gaussian iterations, $\gamma = 0.05$, $R_\kappa = 12$, and 200 curvature iterations.

### 2.2.5 Deep Learning

Using a machine learning-based approach, Rabbani *et al.* (2023) presented an innovative method to measure the contact angle focused on sub-samples of the image around the three-phase contact point. This method generates input data (sub-samples) that selectively excludes nonessential information, thereby minimizing the presence of irrelevant data that can reduce the effectiveness of the deep learning algorithm. To generate the sub-samples data, the contact line is

tracked using a $2^3$ voxel sliding window technique, and contact points are randomly selected (Fig. 6 A) on the contact line to create sub-samples of spherical shape (Fig. 6 B). The sub-sample size is an essential parameter for accurate measurements. If the radius is too small, there may not be sufficient data points for the algorithm, and if the radius is too large, it could introduce irrelevant information that may deviate from the measurement. In this way, the author chooses to use sub-samples with radii of 8 and 4 voxels for the training dataset (Fig. 6 C). The algorithm was trained using the mean square error as the loss function on synthetic droplet images (similar to those used for the Benchmark test described in Section 2.), varying the droplet size, contact angle, and rotating the image. Finally, after the generated sub-samples around the selected contact points, contact angle value are provided based on the dataset training.

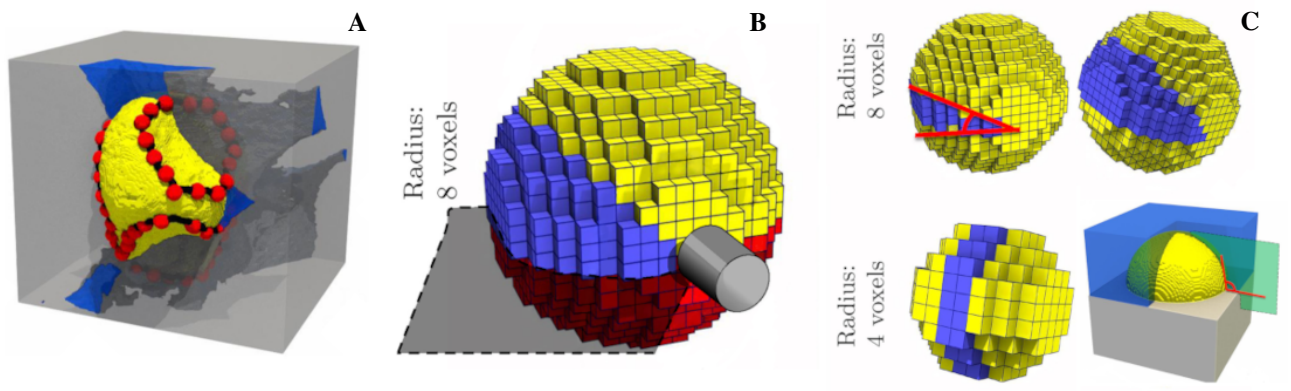


Figure 6. Deep Learning measurement process: (**A**) tracking of the contact line (black points) and selection of randomized contact points (red points over the black points); (**B**) sub-sample generated for the contact angle measurement; (**C**) input data for training the algorithm. Adapted from Rabbani *et al.* (2023).

The present work utilizes the deep learning Python code available on the page (`https://github.com/ArashRabbani/DeepAngle`). The code does not require input measurement parameters.

## 3. RESULTS AND DISCUSSION

The benchmark tests are conducted for resolutions of $1/14^{th}$, $1/28^{th}$, $1/56^{th}$, and $1/112^{th}$, with angles ranging from 0º to 170º, spaced by 10º. The 0º angle corresponds to a sphere resting on a plane, while the 180º angle represents complete wetting of the fluid on the plane. The 180° angle is excluded from the analysis since no contact point can be identified in the segmented image.

Figures 7, 8, and 9 show the analytical angle compared to the mean measured angle $(\hat{\theta})$ for the cases P-Z, P-ZX, and P-ZXY, respectively. These figures present the results obtained by each methodology at different resolutions, enabling the identification of trends related to the analytical curve. Across all three cases, deviations from the analytical can be observed: both Klise *et al.* (2016) and Rabbani *et al.* (2023) show deviations with values greater than the analytical angle, while Scanziani *et al.* (2017) exhibits deviations with values lower than the analytical angle. The results presented of McClure *et al.* (2016) show an increasing trend of deviations for angles exceeding 90º.

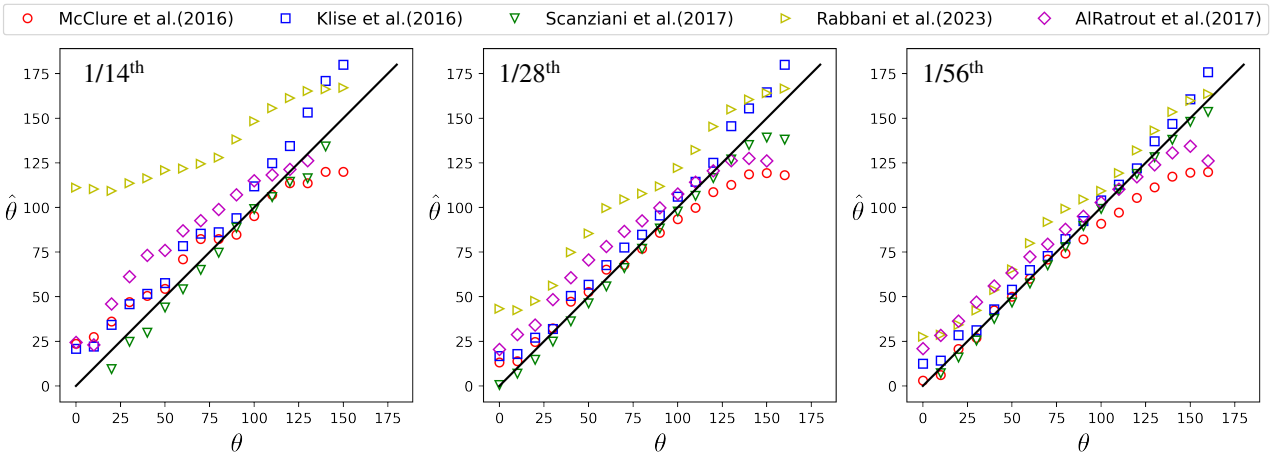


Figure 7. Analytical contact angle comparison for the case P-Z at the resolutions $1/14^{th}$, $1/28^{th}$, and $1/56^{th}$ of the sphere diameter.

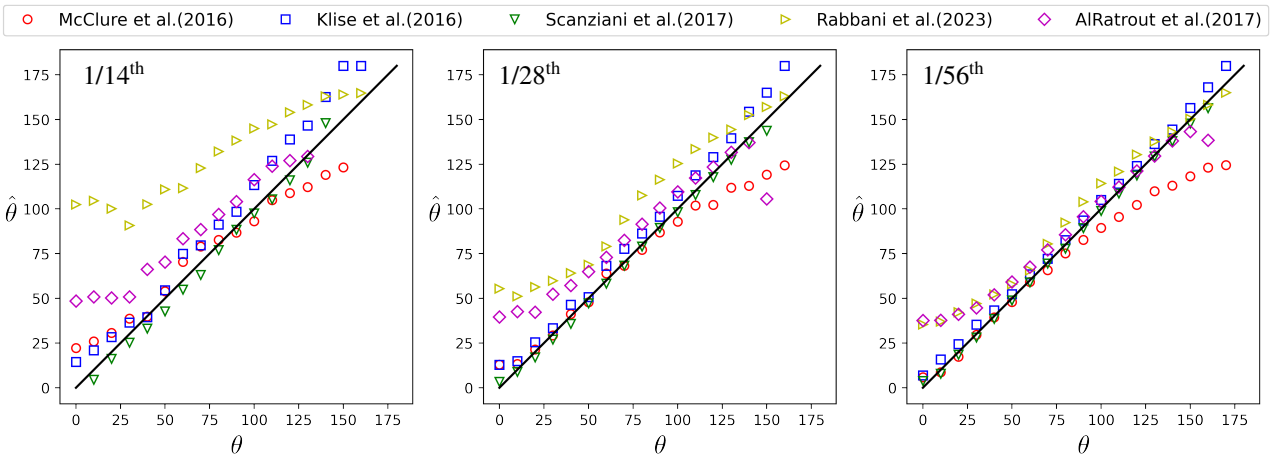


Figure 8. Analytical contact angle comparison for the case P-ZX at the resolutions 1/14th, 1/28th, and 1/56th of the sphere diameter.

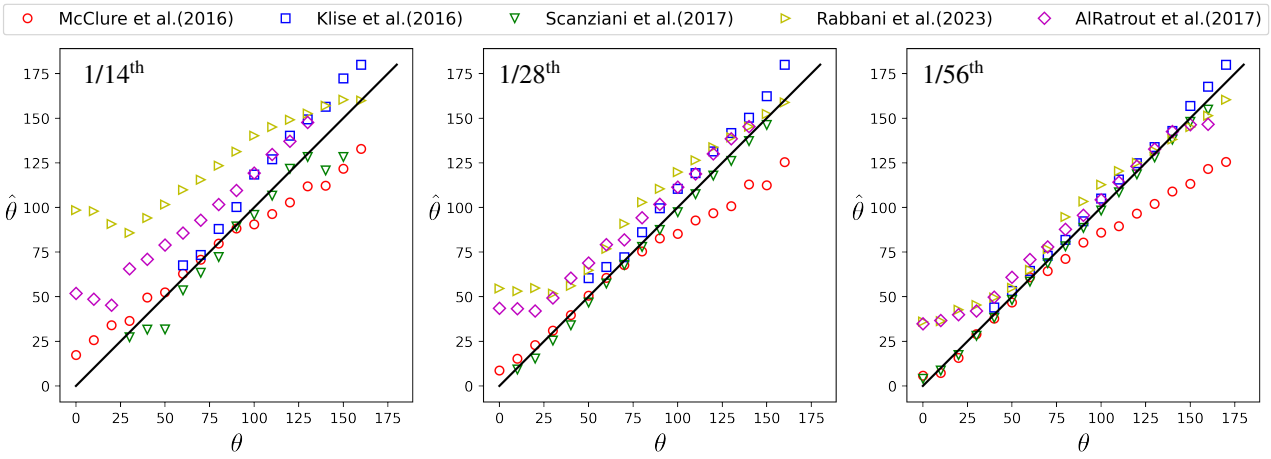


Figure 9. Analytical contact angle comparison for the case P-ZXY at the resolutions 1/14th, 1/28th, and 1/56th of the sphere diameter.

Additionally, it is worth noting that Klise *et al.* (2016) cannot find contact points in the case P-ZXY (Figure 9) for analytical angles less than 60°, 50°, and 40° at resolutions of 1/14th, 1/28th, and 1/56th, respectively. This issue arises from the utilization of 6 voxels connectivity using one fluid as a reference. Nonetheless, this limitation was not evident in the result reported by Klise *et al.* (2016) for the same case P-ZXY.

In a quantitative comparison between methods, four parameters are calculated for each case and resolution: the Mean Signed Difference (MSD)

$$MSD = \frac{1}{n}\sum_{i=1}^{n}\hat{\theta}_i - \theta_i, \tag{4}$$

the Root Mean Squared Deviation (RMSD)

$$RMSE = \sqrt{\frac{\sum_{i=1}^{n}(\hat{\theta}_i - \theta_i)^2}{n}}, \tag{5}$$

the mean standard deviation

$$\hat{\sigma} = \frac{1}{n}\sum_{i}^{n}\sigma_i = \frac{1}{n}\sum_{i}^{n}\underbrace{\left(\sqrt{\frac{\sum_{j=1}^{N}(\theta_{mj} - \hat{\theta})^2}{N-1}}\right)_i}_{\sigma_i}, \tag{6}$$

and the mean of measurement density, being the measurement density ($\lambda$) given by the number of measurements made

divided by the total analytical length of the contact line

$$\hat{\lambda} = \frac{1}{n}\sum_{i}^{n}\lambda_i = \frac{1}{n}\sum_{i}^{n}\underbrace{\left(\frac{N}{2\pi R\sin\theta}\right)_i}_{\lambda_i}, \tag{7}$$

where $\theta_m$ is the contact angle measured in the contact point of image, $N$ total number of points measured in image, $\hat{\theta}_i = \sum_j^N(\theta_{mj})/N$ the mean measured angle (same value presented in the Figures 7, 8, and 9), $\theta_i$ the analytic angle for each case, $n$ the total number of cases analysed varying the analytic angle from 0° to 170º in increments of 10º, and $R$ the droplet radius.

The results of MSD and RMSD for each method are presented in Table 1. The values observed for Klise *et al.* (2016), Scanziani *et al.* (2017), Rabbani *et al.* (2023), and AlRatrout *et al.* (2017) demonstrate clear convergence with an increase in resolution. However, the values obtained for McClure *et al.* (2016) do not converge. In terms of accuracy, Scanziani *et al.* (2017) present lower values of MSD and RMSD, followed by Klise *et al.* (2016), Rabbani *et al.* (2023), and AlRatrout *et al.* (2017). In terms of accuracy, Scanziani *et al.* (2017) achieved lower values of MSD and RMSD, followed by Klise *et al.* (2016), Rabbani *et al.* (2023), and AlRatrout *et al.* (2017) in increasing order of MSD and RMSD values.

Table 1. Comparative analysis for mean signed difference (MSD), root mean squared deviation (RMSD), mean standard deviation ($\hat{\sigma}$), and mean of the measurement density ($\hat{\lambda}$).

| | | MSD | | | | RMSD | | | | $\hat{\sigma}$ | | | | $\hat{\lambda}$ | | | |
|---|---|---|---|---|---|---|---|---|---|---|---|---|---|---|---|---|---|
| | | 1/14$^{th}$ | 1/28$^{th}$ | 1/56$^{th}$ | 1/112$^{th}$ | 1/14$^{th}$ | 1/28$^{th}$ | 1/56$^{th}$ | 1/112$^{th}$ | 1/14$^{th}$ | 1/28$^{th}$ | 1/56$^{th}$ | 1/112$^{th}$ | 1/14$^{th}$ | 1/28$^{th}$ | 1/56$^{th}$ | 1/112$^{th}$ |
| Klise *et al.* (2016) | P-Z | 15.7 | 9.3 | 5.6 | 3.7 | 17.4 | 10.6 | 6.9 | 4.5 | 2.8 | 1.9 | 1.8 | 1.0 | 0.84 | 0.94 | 1.05 | 1.15 |
| | P-ZX | 14.5 | 8.9 | 5.2 | 3.5 | 16.2 | 10.2 | 6.1 | 4.2 | 4.6 | 2.3 | 2.0 | 1.3 | 0.52 | 0.62 | 0.64 | 0.76 |
| | P-ZXY | 14.6 | 9.2 | 5.1 | 3.3 | 16.2 | 10.3 | 5.9 | 4.0 | 3.6 | 1.7 | 1.8 | 0.9 | 0.27 | 0.34 | 0.40 | 0.47 |
| Scanziani *et al.* (2017) | P-Z | -6.1 | -4.9 | -2.4 | -2.4 | 7.0 | 6.9 | 2.9 | 5.2 | 6.5 | 3.8 | 3.3 | 4.3 | 1.20 | 1.63 | 2.10 | 2.34 |
| | P-ZX | -4.9 | -3.5 | -1.8 | -1.5 | 6.1 | 5.3 | 2.4 | 3.8 | 7.1 | 5.0 | 4.5 | 3.9 | 1.63 | 1.52 | 1.89 | 1.94 |
| | P-ZXY | -5.8 | -3.4 | -1.7 | -1.6 | 7.8 | 4.7 | 2.4 | 4.3 | 6.4 | 4.6 | 3.3 | 4.5 | 1.03 | 1.39 | 1.49 | 1.55 |
| Rabbani *et al.* (2023) | P-Z | 62.7 | 29.3 | 15.7 | 9.5 | 67.2 | 30.1 | 16.4 | 10.9 | 0.0 | 0.4 | 1.1 | 1.6 | 0.92 | 0.99 | 1.02 | 1.06 |
| | P-ZX | 59.2 | 27.9 | 14.9 | 8.7 | 63.3 | 29.4 | 16.4 | 11.0 | 0.2 | 2.2 | 3.4 | 4.6 | 0.90 | 0.97 | 0.93 | 1.03 |
| | P-ZXY | 56.0 | 26.0 | 14.0 | 7.7 | 60.6 | 28.1 | 16.1 | 10.1 | 0.5 | 3.0 | 4.7 | 5.7 | 0.63 | 0.68 | 0.55 | 0.61 |
| AlRatrout *et al.* (2017) | P-Z | 18.6 | 8.9 | 4.2 | 3.6 | 21.4 | 15.5 | 14.6 | 12.2 | 0.1 | 0.4 | 1.2 | 1.5 | 1.06 | 1.13 | 1.17 | 1.20 |
| | P-ZX | 19.9 | 9.8 | 5.8 | 4.3 | 23.0 | 18.3 | 14.8 | 12.0 | 2.2 | 2.5 | 2.5 | 3.5 | 1.35 | 1.41 | 1.46 | 1.77 |
| | P-ZXY | 22.2 | 12.2 | 6.7 | 4.8 | 24.9 | 18.8 | 14.4 | 12.0 | 1.6 | 2.4 | 2.4 | 2.8 | 1.42 | 1.46 | 1.47 | 1.50 |
| McClure *et al.* (2016) | P-Z | 1.82 | -6.46 | -9.53 | -14.0 | 14.8 | 15.5 | 15.4 | 19.8 | 2.7 | 4.0 | 3.5 | 3.6 | 4.78 | 4.63 | 4.97 | 4.43 |
| | P-ZX | 0.64 | -7.13 | -11.0 | -13.7 | 14.1 | 15.4 | 17.2 | 19.6 | 4.3 | 5.0 | 4.3 | 4.3 | 5.68 | 5.68 | 5.40 | 5.37 |
| | P-ZXY | -1.1 | -8.26 | -12.3 | -14.2 | 14.8 | 16.3 | 18.6 | 20.0 | 5.9 | 5.7 | 5.8 | 6.1 | 6.97 | 6.49 | 6.25 | 6.09 |

Extending the comparison for the mean standard deviation, Klise *et al.* (2016) was the only one to consistently demonstrate convergence with increasing resolution. Scanziani *et al.* (2017) exhibited convergence only in the case P-ZX, while P-Z and P-ZXY diverge only for the case of 1/112$^{th}$. Both the methodologies of Rabbani *et al.* (2023) and AlRatrout *et al.* (2017) consistently diverged with an increase in resolution. The results of McClure *et al.* (2016) exhibited oscillations in the mean standard deviation with no clear trend.

Considering the number of points measured around the droplet, the mean of measurement density is calculated for each method at different resolutions. The methodologies of Klise *et al.* (2016), Scanziani *et al.* (2017), and AlRatrout *et al.* (2017) consistently demonstrate an increase in measured points with increasing resolution. Rabbani *et al.* (2023) shows an increase for the cases P-Z and P-ZX with increasing resolution, while in the case P-ZXY there are fluctuations in the values. McClure *et al.* (2016) demonstrate a decrease for the cases P-ZX and P-ZXY with increasing resolution, while in the case P-Z there are fluctuations in the values. In general, McClure *et al.* (2016) present the higher number of point measured, followed by Scanziani *et al.* (2017), AlRatrout *et al.* (2017), Rabbani *et al.* (2023), and Klise *et al.* (2016) in decreasing order of $\hat{\lambda}$ values.

To better illustrate the measured values and the standard deviation for each methodology, Figure 10 presents the distribution of angles measured for the plane P-ZY with resolutions of 1/28$^{th}$ and 1/112$^{th}$. The $y$ axis represents the error $\epsilon_\theta = \theta - \theta_m$ of each measurement, and the $x$ axis represents the analytical angle ($\theta$) of the benchmark test. For the characterization of the distribution, a linear color gradient was used to represent the distribution of angles measured. The gradient is normalized for each contact angle case.

Analyzing point-to-point in Figure 10, we can observe certain behaviors that were not apparent when looking at average values. Rabbani *et al.* (2023) shows a trend of increasing the standard deviation from extreme angles of 0º and 180º to 90º. For angles higher than 90º, McClure *et al.* (2016) consistently exhibit errors for each measurement. Decreasing the analytical contact angle, AlRatrout *et al.* (2017) demonstrate a trend of error increment. Scanziani *et al.*

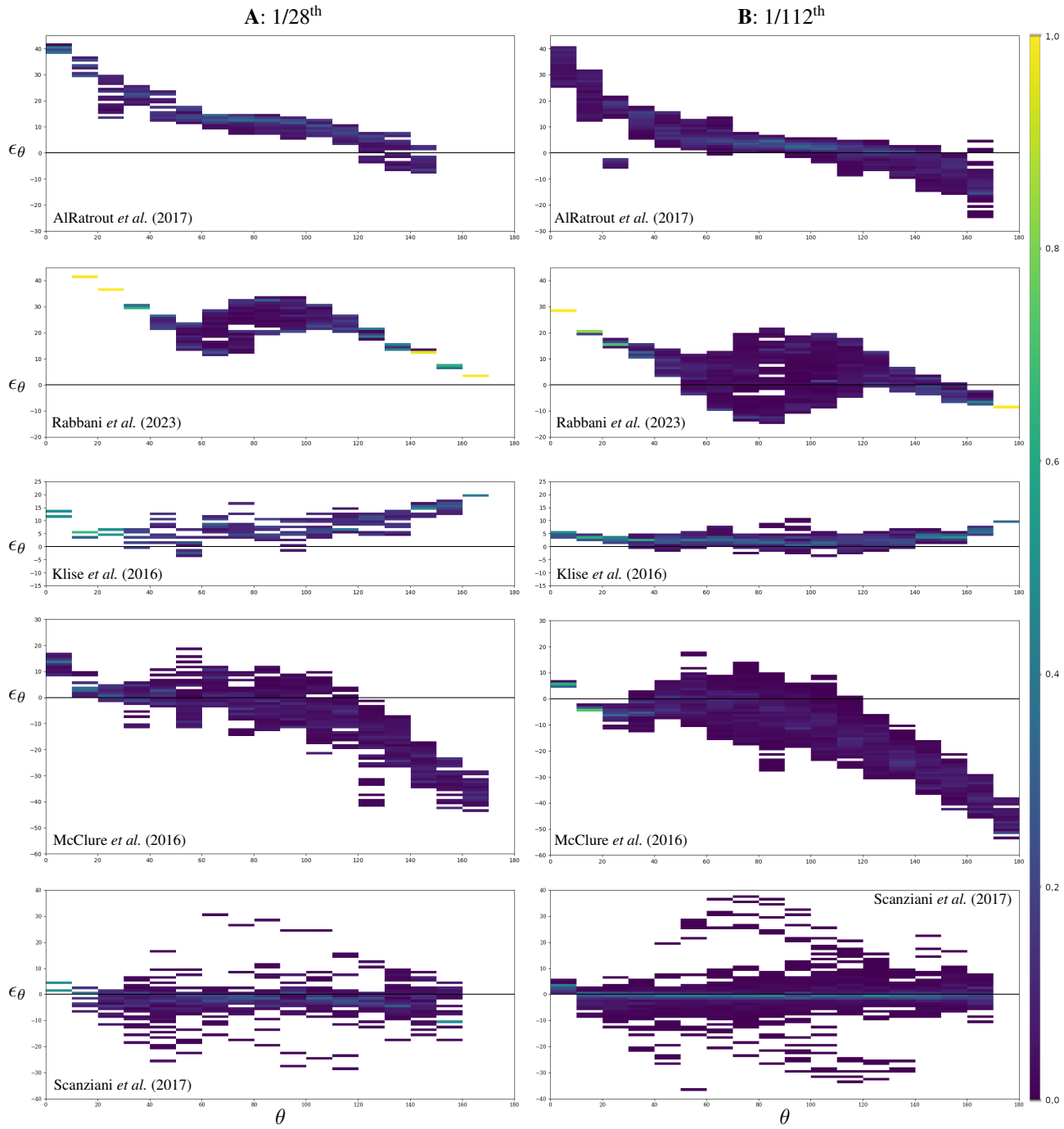


Figure 10. Distribution of contact angle measurement errors for each methodology in the range of analytical angles from 0° to 170° in increments of 10° on the plane P-ZY at resolutions of 1/28th and 1/112th.

(2017) presents a almost constant error deviation for each analytical contact angle. Klise *et al.* (2016) trends to show the smaller standard deviation for all cases.

## 4. CONCLUSION

In this study, we performed a comparative analysis of various methodologies available in the literature for measuring contact angles in porous media using X-ray microtomography images. For this purpose, we employed a benchmark scenario involving a droplet placed on an inclined solid surface with pre-defined contact angles. This approach enabled us to investigate measurement accuracy and precision across different image resolutions.

Among the five compared methodologies, Klise *et al.* (2016) and Scanziani *et al.* (2017) presented the best results, as they were the only ones showing a reduction in errors and standard deviation with increasing resolution. Specifically,

Scanziani *et al.* (2017) achieved the smallest errors, while Klise *et al.* (2016) exhibited the smallest standard deviation. Regarding the application to real porous media segmented data, Scanziani *et al.* (2017) can offer higher accuracy in local measurements at lower resolutions. However, for porous media with wettability variations, Klise *et al.* (2016) may provide a more reliable estimate of these values due to the smaller standard deviation.

For a more comprehensive evaluation of each methodology, we recommend future research that expands the comparative analysis to real microtomography images of porous media with controlled wettability. This would allow for an assessment of the methods in practical applications. Additionally, investigating the impact of solid interface heterogeneity could provide valuable insights.

## 5. ACKNOWLEDGEMENTS

We gratefully acknowledge the support and sponsorship by Equinor Brazil (Project ANP 23270-2). We also acknowledge the support of ANP (Brazil National Oil, Natural Gas and Biofuels Agency) through the R&D levy.

## 6. REFERENCES

AlRatrout, A., Raeini, A.Q., Bijeljic, B. and Blunt, M.J., 2017. "Automatic measurement of contact angle in pore-space images". *Advances in Water Resources*, Vol. 109, pp. 158–169. ISSN 03091708. doi:10.1016/j.advwatres.2017.07.018.

Andrew, M., Bijeljic, B. and Blunt, M.J., 2014. "Pore-scale contact angle measurements at reservoir conditions using x-ray microtomography". *Advances in Water Resources*, Vol. 68, pp. 24–31. ISSN 03091708. doi:10.1016/j.advwatres.2014.02.014.

Chalbaud, C., Robin, M., Lombard, J., Martin, F., Egermann, P. and Bertin, H., 2009. "Interfacial tension measurements and wettability evaluation for geological co2 storage". *Advances in water resources*, Vol. 32, No. 1, pp. 98–109.

Francisca, F.M. and Montoro, M.A., 2015. "Influence of particle size distribution and wettability on the displacement of lnapl in saturated sandy soils". *Journal of Environmental Engineering*, Vol. 141, No. 6, p. 04014091.

Ibekwe, A., Pokrajac, D. and Tanino, Y., 2020. "Automated extraction of in situ contact angles from micro-computed tomography images of porous media". *Computers and Geosciences*, Vol. 137. ISSN 00983004. doi:10.1016/j.cageo.2020.104425.

Klise, K.A., Moriarty, D., Yoon, H. and Karpyn, Z., 2016. "Automated contact angle estimation for three-dimensional x-ray microtomography data". *Advances in Water Resources*, Vol. 95, pp. 152–160. ISSN 03091708. doi:10.1016/j.advwatres.2015.11.006.

McClure, J.E., Berrill, M.A., Gray, W.G. and Miller, C.T., 2016. "Tracking interface and common curve dynamics for two-fluid flow in porous media". *Journal of Fluid Mechanics*, Vol. 796, pp. 211–232. ISSN 14697645. doi:10.1017/jfm.2016.212.

Rabbani, A., Sun, C., Babaei, M., Niasar, V.J., Armstrong, R.T. and Mostaghimi, P., 2023. "Deepangle: Fast calculation of contact angles in tomography images using deep learning". *Geoenergy Science and Engineering*, Vol. 227, p. 211807. ISSN 29498910. doi:10.1016/j.geoen.2023.211807. URL `http://arxiv.org/abs/2211.15243`.

Scanziani, A., Singh, K., Blunt, M.J. and Guadagnini, A., 2017. "Automatic method for estimation of in situ effective contact angle from x-ray micro tomography images of two-phase flow in porous media". *Journal of Colloid and Interface Science*, Vol. 496, pp. 51–59. ISSN 10957103. doi:10.1016/j.jcis.2017.02.005.

Yang, J. and Zhou, Y., 2020. "An automatic in situ contact angle determination based on level set method". *Water Resources Research*, Vol. 56, pp. 1–14. ISSN 19447973. doi:10.1029/2020WR027107.

Zang, C., Wang, L., Zhou, K., Yu, F., Jiang, H. and Li, J., 2023. "Automatic measurement of three-phase contact angles in pore throats based on digital images". *Petroleum Exploration and Development*, Vol. 50, pp. 442–449. ISSN 18763804. doi:10.1016/S1876-3804(23)60399-4.

## 7. RESPONSIBILITY NOTICE

The authors are solely responsible for the printed material included in this paper.